Proceedings of the Combustion Institute 40 (2024) 105315

Contents lists available at ScienceDirect

Proceedings of the Combustion Institute

journal homepage: www.elsevier.com/locate/proci

Particle-resolved numerical simulations of char particle combustion in isotropic turbulence

Kaiyue Wang, Haiou Wang *, Jian Zheng, Kun Luo, Jianren Fan

State Key Laboratory of Clean Energy Utilization, Zhejiang University, Hangzhou 310027, PR China

ARTICLE INFO

Keywords:
Numerical simulation
Particle-resolved
Turbulent particle combustion
Drag force

ABSTRACT

In the present study, two-dimensional particle-resolved numerical simulations of char particle combustion are performed. A series of cases are considered, with varying turbulence intensities and heterogeneous reaction rates. The impact of turbulence and Stefan flow on char particle combustion is examined. It is shown that the cases with higher turbulence intensity and heterogeneous reaction rate exhibit higher mean gas-phase temperatures and reaction rates. The range of the Stefan flow Reynolds number (Re_S) increases as the value of heterogeneous reaction rate increases. Additionally, higher turbulence intensity is associated with an increased range of Re_S. The drag force coefficient of burning particles is analyzed. The results show that turbulence induces fluctuations of drag force coefficient, and increasing the turbulent velocity broadens the drag force coefficient fluctuation amplitude. The particle drag force is increased with increasing heterogeneous reaction rate. The pressure and viscous components of the drag force are examined. It is revealed that the increase of heterogeneous reaction rate alters the pressure distribution on the particle surface, resulting in the increase of pressure drag force, while the viscous drag force remains almost unchanged.

1. Introduction

Coal combustion is prevalent and crucial in industrial applications including furnace, fluidized bed boiler and coke oven [1–3]. However, coal combustion produces harmful pollutant, such as NO_x, SO_2 and particulate matter. Moreover, the combustion of coal releases significant amount of greenhouse gases such as carbon dioxide, which influences the surface temperature of the earth and the climate. Thus, it is important to design high-efficiency and low-emission combustion systems, which requires improved fundamental understanding of coal combustion. In applications, coal is firstly pulverized into fine particles, and particle combustion occurs in turbulent flows. However, existing understanding of turbulent particle combustion is insufficient and more fundamental studies are required to develop advanced modeling tools and combustion systems.

Previous studies have been conducted experimentally to understand the characteristics of particle combustion [4–8]. Hwang et al. [4] measured a laboratory-scale pulverized coal jet flame. They observed that in the upstream region, combustion is limited to the periphery of the particle cluster, whereas in the downstream region, combustion also takes place within the coal particle cluster. Toporov et al. [5] investigated oxy-fuel pulverized coal swirling flames and discovered an internal recirculation zone that provides high temperature products back toward the burner inlet and facilitates the particle ignition. Balusamy and Hochgreb [7,8] conducted experiments of particle-laden swirling flames in air and oxy-fuels. It was observed that the replacement of N_2 with CO_2 reduces the flame intensity since the heat capacity of CO_2 is higher than N_2. Although these studies are helpful to understand particle combustion, it is challenging to attain the detailed flow and flame structures in particle combustion by experiments.

Numerical simulation is a promising approach for studying particle combustion as it provides detailed information of turbulence and chemical reactions. The numerical methods of particle combustion can be categorized into two types, including the point-particle method [9] and particle-resolved method [10]. The point-particle method tracks the particles in a Lagrangian way without considering the volume effects. In contrast, the particle-resolved method considers the volume of particles and can resolve the surface of particles. The majority of previous numerical studies of particle combustion have utilized point-particle methods [9,11–14].

In order to obtain the information at the particle scale, particularly to reveal the physical processes within the particle boundary layer, the particle-resolved approach is required. A few numerical investigations have been performed for this purpose [15–20]. Luo et al. [15] modeled a single char particle combustion with different temperatures and inflow Reynolds numbers. It was found the dominant reaction

* Corresponding author.
E-mail address: wanghaiou@zju.edu.cn (H. Wang).

https://doi.org/10.1016/j.proci.2024.105315
Received 4 December 2023; Accepted 31 May 2024
Available online 24 June 2024

on the particle surface transitioned from oxidation to gasification of char and carbon dioxide as temperature increases. Farazi et al. [17] studied the combustion of a single char in oxygen and oxygen-enriched atmospheres. They found that under laminar conditions, both the convective and diffusive Damkhöler numbers were greater than unity, indicating that the influence of convective transport cannot be ignored. Tufano et al. [20] investigated the combustion of multiple particles and revealed a strong dependence of flame interaction on the particle distance.

In the combustion process of particles, heterogeneous reactions can induce a surface mass flow, known as Stefan flow, on the particle surface. The presence of Stefan flow alters the exchange of energy and momentum between the particle and fluid. However, most existing point-particle models for coal combustion do not account the impact of Stefan flow, and the model performance can be deteriorated. In response to this issue, a few studies have been carried out [16,18,21]. Jayawickrama et al. [18] investigated the influence of Stefan flow on particle Nusselt number, and developed a model to take this influence into account. Luo et al. [16] developed a model to describe the impact of Stefan flow on particle drag force. Dierich et al. [21] introduced the transport of components within the porous structure inside the particles and observed the existence of Stefan flow within the particle interior, demonstrating its significant role in the mass transfer process.

The aforementioned particle-resolved numerical studies were conducted under laminar flow conditions. However, in practical industrial devices, particle combustion often takes place in a turbulent environment. The particle-resolved simulations of turbulent particle combustion have been rarely reported. The impacts of turbulence and Stefan flow on particle-resolved combustion are still open questions which require further explorations. In this context, direct numerical simulations of particle combustion in isotropic turbulence are conducted with the particle-resolved method in this work. The contents of the paper are as follows. First, the configuration and particle-resolved method are described. Second, the characteristics of scalar fields and reaction rates are examined. Finally, the influence of turbulence intensity and heterogeneous reaction on the drag force is scrutinized.

2. Configuration and numerical methods

2.1. Simulation configuration

In the present work, two-dimensional particle-resolved numerical simulations of char particle combustion are performed under turbulent conditions. The char particles are randomly distributed within the computational domain, and their locations are fixed during the simulations. The particle diameter D_p is initially set as 400 μm, which is consistent with the particle size used in previous experimental [22] and numerical [23] studies. The initial temperature of the gas and solid phases is 1500 K to facilitate the chemical reactions of the char particles [15]. The number of particles in the computational domain is 128. The computational domain is a two-dimensional square box with $L_x \times L_y = 48D_p \times 48D_p$. A uniform grid is used with a grid size of $\Delta = D_p/50$. The resultant grid number is $N_x \times N_y = 2400 \times 2400$. Periodic boundary conditions are imposed in both the x and y directions.

Homogeneous isotropic turbulence based on a Passot–Pouquet kinetic energy spectrum [24] is used as the initial turbulence field. To study the impact of turbulence intensity on char particle combustion, the turbulent velocity u' is varied while maintaining a consistent integral length scale $l_t = 1.62$ mm. The values of turbulent velocities in various cases are shown in Table 1. The grid resolution is sufficient to resolve all the turbulence scales. Fig. 1 shows a schematic of the computational domain, where the particles are also superimposed. Note that a representative particle is highlighted in the plot, which is selected for further analyses of the flow and combustion characteristics around a single particle in Section 3.

Table 1
Parameters of various cases.

Case	B/B_0	u' (m/s)	Case	B/B_0	u' (m/s)
1	0	8.1	7	0	16.2
2	0.1	8.1	8	0.1	16.2
3	0.5	8.1	9	0.5	16.2
4	1.0	8.1	10	1.0	16.2
5	1.5	8.1	11	1.5	16.2
6	2.0	8.1	12	2.0	16.2

Table 2
Kinetic parameters of chemical reactions.

Chemical reaction	B_0	E (J/mol)
$2C(s) + O_2 \rightarrow 2CO$	1.97×10^7	1.98×10^5
$C(s) + CO_2 \rightarrow 2CO$	1.29×10^5	1.91×10^5
$2CO + O_2 \rightarrow 2CO_2$	2.29×10^{12}	167×10^5

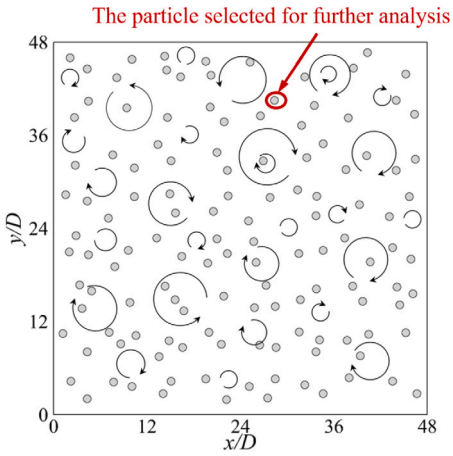

Fig. 1. The schematic of the computational domain superimposed with particles. A representative particle for further analysis of the flow and combustion characteristics around a single particle in Section 3 is also highlighted.

The combustion process is characterized by two semi-global heterogeneous reaction mechanisms for char conversion and a homogeneous reaction for CO oxidation. The kinetic parameters for these chemical reactions are provided in Table 2. The above mechanisms have been validated in previous studies [15,16,25]. In this study, the gas phase consists of N_2, O_2, CO, and CO_2, while the water gas shift reaction is neglected. A similar method was implemented in Refs. [15,16]. A total of twelve cases are simulated in the present work. Specifically, cases 1~6 are performed with a turbulent velocity of 8.1 m/s, while the turbulent velocity for cases 7~12 is 16.2 m/s. To examine the impact of Stefan flow on char particle combustion, it is essential to adjust the reaction rates of particles, which is enabled by artificially modifying the pre-exponential factors, B, as listed in Table 1. Note that only the rates of heterogeneous reactions are varied in various cases while those of the homogeneous reactions remain unchanged.

2.2. Numerical methods

In the present work, the immersed boundary method is used for resolving the particles [26]. Moreover, the improved ghost cell immersed boundary method is implemented to enforce the constrains of velocity and temperature. Note that the grid size of the simulations, *i.e.* $\Delta = D_p/50$, is smaller than those of previous studies with direct force immersed boundary method [27,28]. This is because that the ghost cell immersed boundary method requires a higher resolution to ensure mass conservation at the particle surface to accurately resolve the particle boundary layer. A brief introduction of the improved ghost cell

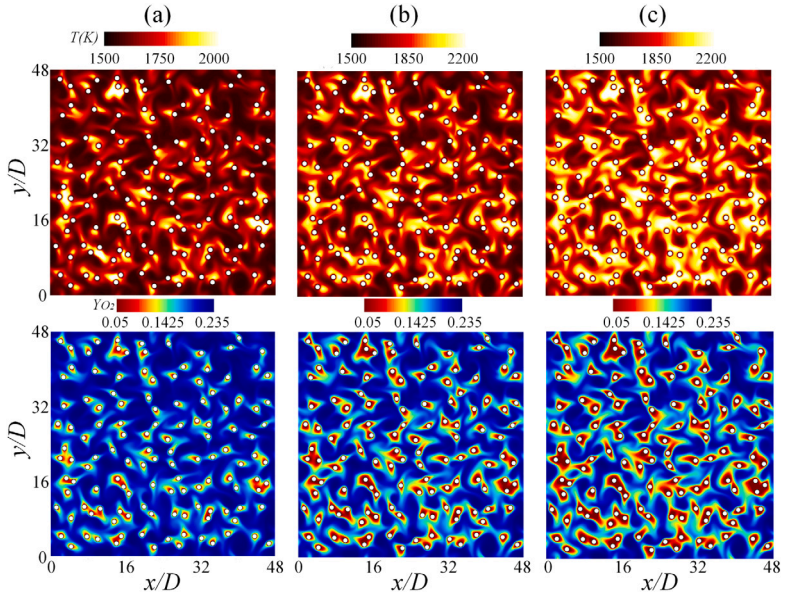

Fig. 2. The distributions of (top) temperature and (bottom) O_2 mass fraction for the cases with u' = 16.2 m/s and various heterogeneous reaction rates: (a) B/B_0 = 0.5, (b) B/B_0 = 1.0 and (c) B/B_0 = 2.0.

immersed boundary method is given below. More detailed description and validation of the method can be found in Refs. [15,16].

The convective and diffusive mass flux of gas-surface species at the surface are balanced by the production (or consumption) rate of gas-phase species by surface reactions. This relationship is:

$$\bar{n} \cdot [\rho Y_k (V_k + u_{Ste})] = \dot{m}_k \tag{1}$$

where $\bar{n}$ represents the outward wall-normal unit vector, and $\dot{m}_k$ is the mass production rate of the kth species. u_{Ste} represents the velocity of the Stefan flow. The diffusion velocity of the kth species is related to the gradient of the species mass fraction as:

$$V_k = \frac{1}{X_k \overline{W}} \sum_{j \neq k} W_j D_{k,j} \nabla X_j \tag{2}$$

The total species diffusion flux is zero:

$$\sum_k V_k Y_k = 0. \tag{3}$$

Based on mass transfer balance at the surface, the Stefan flow velocity can be formulated as

$$\bar{n} \cdot u_{Ste} = \frac{1}{\rho} \sum_{k=1}^{K_g} \dot{m}_k. \tag{4}$$

The boundary velocity of the particle, u_B, is a combination of particle shrinking velocity, v_n, and the Stefan flow velocity, which is given by

$$u_B = u_{Ste} + v_n = u_{Ste} + \frac{\int_{surf} \dot{m}_c ds}{s \rho_c} \tag{5}$$

Here ds is surface element of the particle, and ρ_c is the density of the char particle.

In this work, the temperature gradient within the particle is neglected. Therefore, the heat transfer at the interface contains the diffusive flux, radiation, reaction heat and the heat conduction from the outside of the particle. The particle energy balance is then given by

$$V_{C_{p,C}} \frac{dT_p}{d\tau} = \int_s (-\sigma \varepsilon (T_p^4 - T_0^4) + \sum_{k=1}^{K} \dot{m}_k h_k + \bar{n} \cdot \lambda \nabla T_{gas}) ds \tag{6}$$

where V is the volume of the particle, T_0 represents the temperature of the incoming flow, and $c_{p,C}$ is the heat capacity of the char particle. In the radiation term, ε is the emissivity coefficient, and σ is the Stefan–Boltzmann constant. $\dot{m}_k$ and h_k are the reaction rate and enthalpy of species k, respectively.

This study employs Pencil Code [29], a compressible solver, to solve the non-conservative form of the Navier–Stokes equations. The governing equations consist of the continuity equation, the momentum equation, the species transport equation, the energy equation in terms of temperature, and the ideal gas state equation. A sixth-order central difference scheme was used for spatial discretization, and a three-step third-order Runge–Kutta scheme was used for time stepping.

3. Result and discussion

3.1. General characteristics

Fig. 2 presents the distributions of temperature and Y_{O_2} at t = 0.2 ms for the cases with u' = 16.2 m/s and various heterogeneous reaction rates. As can be seen, heterogeneous reaction significantly affects the scalar fields. For the case with B/B_0 = 0.5, the maximum temperature remains relatively low, which is only 2000 K. As B/B_0 increases to 1.0 and 1.5, the maximum temperature rises to 2200 K. Notably, the high-temperature region is the largest in the case with B/B_0 = 1.5. The impact of heterogeneous reaction on the O_2 distribution is also significant. Around the particles, O_2 is consumed. For the cases with low values of B/B_0, O_2 is only partially consumed, while for the cases with high values of B/B_0, the concentration of O_2 near the particles is negligible, indicating that O_2 is completely consumed. It is interesting to observe that the particle distribution influences the combustion characteristics. In particular, single particle combustion is observed when the particle is away from others while group combustion [30] is more likely to occur with particles being close to each other.

To quantify the effects of heterogeneous reaction and turbulence on temperature, the temporal evolutions of the averaged gas-phase temperature, $\overline{T}_g$, is displayed in Fig. 3. In the early stage of combustion, $\overline{T}_g$ increases slowly. At around t = 0.1 ms, $\overline{T}_g$ starts to rise rapidly. After t = 0.2 ms, the temperature growth rate slows down for the cases with high heterogeneous reaction rates ($B/B_0 \geq 1.0$). The impact of turbulence intensity on temperature is also apparent. For the cases with the same value of B, the temperature is higher in the case with a higher turbulence intensity, which can be attributed to the enhancement in the

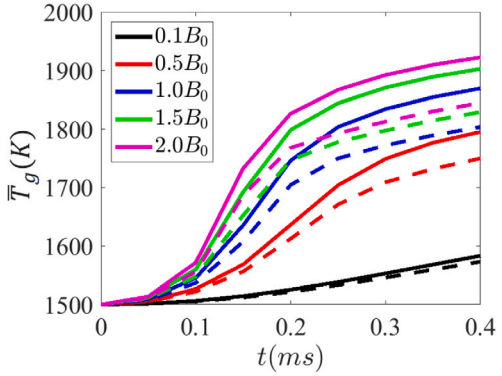

Fig. 3. The temporal evolutions of the averaged gas-phase temperature for cases with various heterogeneous reaction rates B. The dashed lines denote the cases with u' = 8.1 m/s, the solid lines denote the cases with u' = 16.2 m/s.

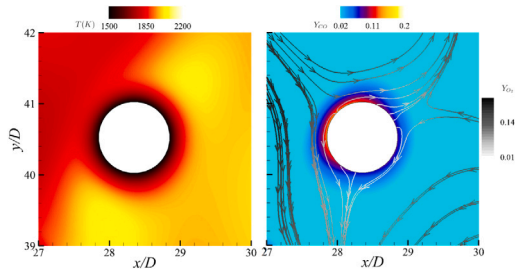

Fig. 4. The distributions of (left) temperature and (right) CO mass fraction around the representative particle for the case with u' = 16.2 m/s and B/B_0 = 1.5 at t = 0.4 ms.

reaction rates by turbulent mixing, as will be quantified in Section 3.2.

Particle-scale features of particle combustion are also revealed. Fig. 4 shows the temperature and CO mass fraction distributions around the representative particle (see Fig. 1) for the case with u' = 16.2 m/s and B/B_0 = 1.5 at t = 0.4 ms. The char is oxidized to produce CO at the particle surface. The surrounding fluid entrains the Stefan flow and carries it away. During this process, the reaction between CO and O_2 results in the production of a large amount of CO_2, and high-temperature regions are observed at certain distances from the particle.

3.2. Statistics of reaction rate

In the following, variation of species reaction rates as well as the pressure around the circumference of a particle is examined for various cases. Fig. 5 shows the instantaneous profiles of the reaction rates for C, O_2 and CO and the pressure around the circumference of the representative particle at t = 0.4 ms. As can be seen, the profiles exhibit multiple peaks and valleys, which is different from those in laminar flows [15,16]. This can be attributed to the stochastic nature of turbulence, causing particles to interact with incoming flows from various directions. Comparison between the cases with different turbulence intensities reveals that the magnitude of the species reaction rate increases with increasing turbulence intensity. Moreover, it is shown that, as B/B_0 increases, the species reaction rate magnitude is also increased, as expected. Note that particle combustion also alters the pressure distribution on the particle surface, which impacts the drag force of the particle, as will be further discussed in Section 3.3.

To gain further insights into the characteristics of char particle combustion, the temporal evolutions of mean species reaction rates of all particles are presented in Fig. 6. The results show that for the cases with B/B_0 = 0.1, the mean species reaction rates first increase and then

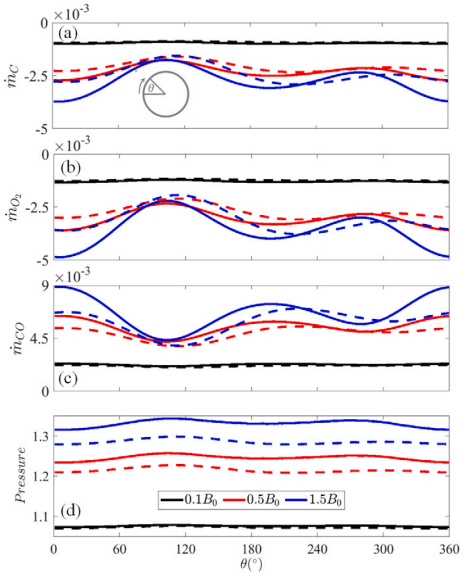

Fig. 5. The instantaneous profiles of the reaction rates and pressure around the circumference of the representative particle for the cases with B/B_0 = 0.1, 0.5 and 1.5 at t = 0.4 ms. The dashed lines denote the cases with u' = 8.1 m/s, the solid lines denote the cases u' = 16.2 m/s.

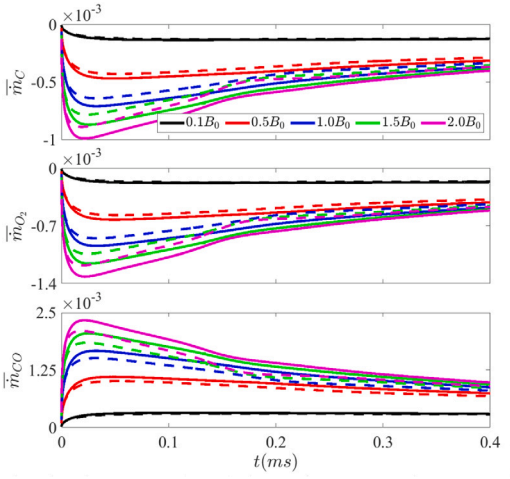

Fig. 6. The temporal evolutions of mean reaction rates of all particles for cases with various B at t = 0.4 ms. The dashed lines denote the cases with u' = 8.1 m/s, the solid lines denote the cases with u' = 16.2 m/s.

plateaus at a relatively low level. In contrast, the mean species reaction rates grow rapidly in the early stage of combustion for the cases with $B/B_0 \geq 0.5$. After reaching a peak within a short time, the mean species reaction rates decline. Moreover, a higher value of heterogeneous reaction rate leads to a higher peak of the mean species reaction rates. The differences of the mean species reaction rate evolutions caused by varying heterogeneous reaction rates can be explained as follows. In the cases with B/B_0 = 0.1, the low heterogeneous reaction rates result in slow consumptions of O_2. This allows for sustained reactions over a long time due to the relatively abundant of O_2. In contrast, for the cases with $B/B_0 \geq 0.5$, the rapid consumption of O_2 prevents the particles from sustaining high reaction rates.

In char particle combustion, it is of considerable interest to study the Stefan flow by modifying the heterogeneous reaction rate. The Stefan flow Reynolds number, Re_S, is introduced, which is calculated as:

$$Re_S = \frac{D_p \iint_{S_p} \dot{m}_c ds}{\rho_c \nu_c}. \quad (7)$$

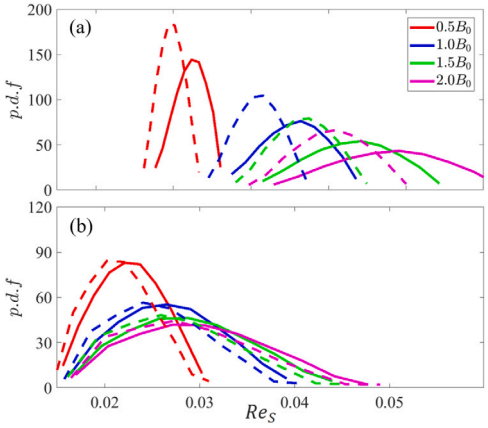

Fig. 7. The probability density function of Stefan Reynolds number for the cases with various B at (a) t = 0.1 ms and (b) t = 0.4 ms. The dashed lines denote the cases with u' = 8.1 m/s, the solid lines denote the case u' = 16.2 m/s.

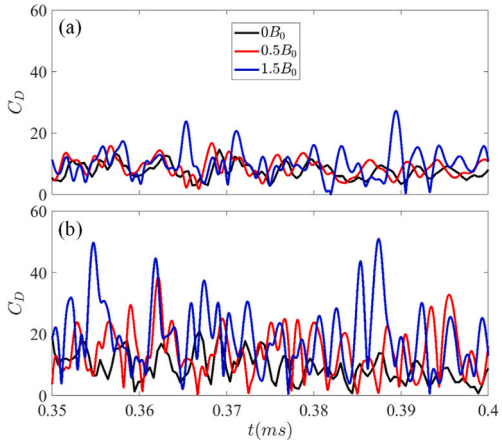

Fig. 8. The temporal evolutions of drag coefficient for the representative particle for the cases with B/B_0 = 0, 0.5, 1.5 and (a) u' = 8.1 m/s and (b) u' = 16.2 m/s.

where ρ_c and ν_c are the characteristic density and viscosity of the fluid, respectively. We note that, near burning particles, the distribution of a fluid quantity ϕ is inhomogeneous. To determine the characteristic value of these quantities, *i.e.* ϕ_c, the following equation is employed [31]:

$$\phi_c = \frac{\int e^{-|\mathbf{r}-\mathbf{r_p}|/R}\phi(\mathbf{r})\mathrm{d}\Omega}{\int e^{-|\mathbf{r}-\mathbf{r_p}|/R}\mathrm{d}\Omega}, \tag{8}$$

where $\mathbf{r}$ is the location of the fluid near the particle, $\mathbf{r_p}$ is the location of the particle center, and R is the radius of the particle. The integration is performed over the region near the particle Ω.

Fig. 7 presents the probability density functions for Re_S in various cases. As can be seen, the range of Re_S increases as the value of heterogeneous reaction rate increases. Additionally, higher turbulence intensity is associated with an increased range of Re_S. In Fig. 7(a), the difference in the range of Re_S for various cases is more significant than that in Fig. 7(b). At t = 0.4 ms, as the turbulence decays and the reaction rate decreases, the range of Re_S narrows, and the difference between the cases with different turbulence intensities further diminishes.

3.3. Analysis of drag force of particles

In point-particle simulations, accurate description of the momentum exchanges between the solid phase and the gas phase, which is usually described by the particle drag force, F_D, is essential. In most of the studies using the point-particle method, the drag force of burning particles is considered with empirical formulas, which have been mostly developed from inert conditions [9,14]. The influence of combustion on particles is not considered. Therefore, understanding the drag force of burning particles with the particle-resolved method is of great significance.

The drag force, F_D, contains two contributions, namely the pressure (F_p) and viscous (F_τ) components as :

$$F_D = \int_A P dA + \int_A \tau dA. \tag{9}$$

The drag force coefficient, C_D, is then defined as:

$$C_D = \frac{F_D}{\frac{1}{2}\rho U_r^2}, \tag{10}$$

where U_r is the relative velocity of the fluid surrounding the particle [32].

Fig. 8 shows the variations of C_D for the representative particle under different turbulence intensity and heterogeneous reaction rate conditions over a time interval of 0.05 ms. It is seen that turbulence induces fluctuations of C_D. Increasing the turbulent velocity broadens the amplitude of fluctuation, consistent with the study of inert particles in turbulent flows by Botto and Prosperetti [33]. In comparison to inert particles, C_D of burning particles in turbulent flow oscillates more significantly, and this phenomenon becomes more pronounced with increased values of heterogeneous reaction rate.

In the literature, many models of drag force coefficient have been proposed for numerical simulations using the point-particle method [9, 14]. In the present work, the drag force coefficient model developed for two-dimensional particles obtained through least squares fitting [16], based on the work of Schiller and Naumann [34]:

$$C_D = \frac{24}{Re_p}(0.382 + 0.191 Re_p^{0.678}) \tag{11}$$

is analyzed and the model predictions are compared with the results of the present particle-resolved simulations. Here, Re_p is the particle Reynolds number defined as $Re_p = D_p U_r/\nu_c$.

Fig. 9 displays the scatter plots of C_D as a function of the particle Reynolds number Re_p for various cases at t = 0.4 ms. Note that turbulence intensity evidently affects the values of Re_p. In the cases with low turbulence intensity, the majority of Re_p are below 4.0. In contrast, for high turbulence intensity, the range of Re_p is wider, with the maximum value exceeding 8.0. It can be seen that Eq. (11) predicts well the drag force coefficient in the non-reacting cases, and a negative correlation between the drag force coefficient and the particle Reynolds number is observed. For burning particles, there is still a negative correlation between C_D and Re_p, but Eq. (11) under-estimates the values of C_D. As the heterogeneous reaction rate increases, this phenomenon becomes more noticeable. Hence, we conclude that combustion results in an increase in the drag force of the burning particles in turbulent flows, which is consistent with the finding of burning particles in laminar flows [16].

To understand the mechanism for the increased drag force with increasing heterogeneous reaction rate, the averaged values of the pressure drag force and viscous drag force of various cases are shown in Fig. 10. It is revealed that the drag force components are larger in the cases with high turbulence intensity compared with those with low turbulence intensity. The pressure drag force is substantially larger than the viscous drag force in all cases. Moreover, the pressure drag force is increased considerably in the cases with burning particles, while the viscous drag force remains almost unchanged. Note that Fig. 5 shows that pressure distributions around the burning particles are altered due to reactions, which results in an increase in the pressure component of the drag force. As for the viscous drag force, two factors should be considered. First, the increase in CO and CO_2 in particle combustion

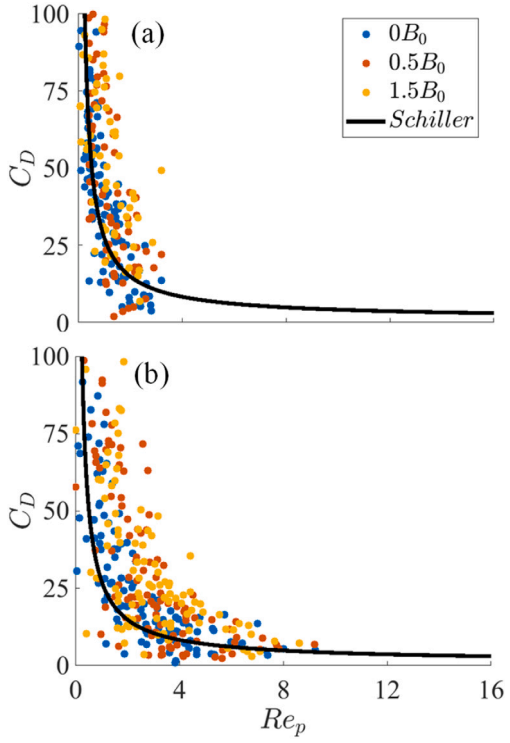

Fig. 9. The scatter plots of drag coefficient with particle Reynolds number for the cases with B/B_0 = 0, 0.5, 1.5 and (a) u' = 8.1 m/s and (b) u' = 16.2 m/s at t = 0.4 ms.

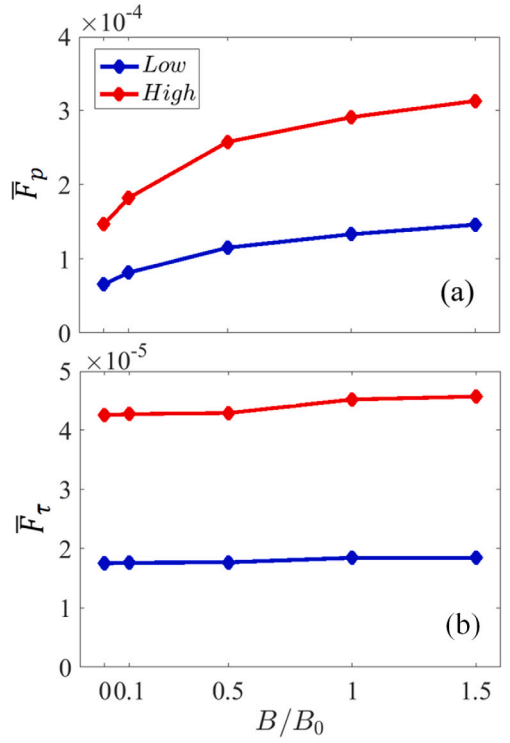

Fig. 10. The averaged values of the pressure drag force and viscous drag force for the cases with B/B_0 = 0, 0.1, 0.5, 1.0 and 1.5.

reduces the viscosity of the fluid. Second, the rise of temperature increases the viscosity of the fluid. The competitions of the two factors lead to a viscous drag force similar to that in the non-reacting case

4. Conclusions

In the present work, two-dimensional particle-resolved numerical simulations of char particle combustion are performed under turbulent conditions for the first time. A series of cases were considered with various turbulence intensities and heterogeneous reaction rates to explore the influence of turbulence and Stefan flow on char particle combustion. The main findings can be summarized as follows.

First, the general characteristics of the scalar fields are examined. It is shown that the cases with a high turbulence intensity exhibit higher temperatures. The impact of heterogeneous reaction on the scalar distributions is also revealed. The mass fraction of oxygen surrounding particles decreases with increased values of heterogeneous reaction rate.

Second, the Stefan flows are examined. The probability density function of Stefan Reynolds number for various cases is presented. It is revealed that the range of Stefan Reynolds number increases as the value of heterogeneous reaction rate increases. Higher turbulence intensity is associated with an increased range of Stefan Reynolds number. Besides, as the turbulence decays and the reaction rate decreases, the range of Stefan Reynolds number narrows.

Finally, the drag force coefficient of burning particles is analyzed. The results show that turbulence induces fluctuations of drag force coefficient and increasing the turbulent velocity broadens the drag force coefficient fluctuation amplitude. Moreover, it is revealed that heterogeneous reactions increase the particle drag force. The two components of the drag force are analyzed, with the pressure drag force being dominant. The pressure drag force is increased considerably in the cases with increased heterogeneous reaction rates, while the viscous drag force remains almost unchanged.

Novelty and significance statement

This paper presents the first particle-resolved numerical simulation of char particle combustion in isotropic turbulence. The novelty of this study lies in that it reports the effects of turbulence intensity and heterogeneous reactions on particle combustion, which has been rarely studied. Both the local and mean reaction rates are analyzed, showing the reaction rates are enhanced with increasing turbulence intensity. Temporal variations of the drag force coefficient for representative particles are examined to understand turbulence and particle combustion impacts on particle drag force. The relationship between the drag coefficient and Reynolds number for burning particles is examined, and the underlying physics are explained. The study is significant as it improves our understandingof burning particles in isotropic turbulent flows, which has important implications to develop accurate models for particle combustion and the design of advanced particle combustion systems.

CRediT authorship contribution statement

Kaiyue Wang: Performed research, Analyzed data, Drafted the paper. **Haiou Wang:** Supervised the project, Designed research, Provided fundings, Reviewed the paper. **Jian Zheng:** Analyzed data, Drafted the paper. **Kun Luo:** Supervised the project, Reviewed the paper. **Jianren Fan:** Supervised the project, Provided fundings, Reviewed the paper.

Declaration of competing interest

The authors declare that they have no known competing financial interests or personal relationships that could have appeared to influence the work reported in this paper.

Acknowledgments

This research was supported by Natural Science Foundation of China (Grant Nos. 51836007 and 52022091).

References

[1] F. Hu, P. Li, T. Zhang, W. Li, K. Wang, J. Guo, J. Mi, Z. Liu, Reaction characteristics and MILD combustion of residual char in a pilot-scale furnace, Energy Fuels 33 (12) (2019) 12791–12800.

[2] D. Rong, M. Horio, DEM simulation of char combustion in a fluidized bed, in: Second International Conference on CFD in the Minerals and Process Industries CSIRO, Melbourne, Australia, 1999, pp. 65–70.

[3] S. Liu, G. Zhu, Y. Niu, L. Wen, Y. Lei, D. Wang, et al., Characteristics of particulate emissions from coal char combustion: Char fragmentation and ash coalescence behaviors, Fuel 310 (2022) 122283.

[4] S.m. Hwang, R. Kurose, F. Akamatsu, H. Tsuji, H. Makino, M. Katsuki, Application of optical diagnostics techniques to a laboratory-scale turbulent pulverized coal flame, Energy Fuels 19 (2) (2005) 382–392.

[5] D. Toporov, P. Bocian, P. Heil, A. Kellermann, H. Stadler, S. Tschunko, M. Förster, R. Kneer, Detailed investigation of a pulverized fuel swirl flame in CO2/O2 atmosphere, Combust. Flame 155 (4) (2008) 605–618.

[6] P. Heil, D. Toporov, H. Stadler, S. Tschunko, M. Förster, R. Kneer, Development of an oxycoal swirl burner operating at low O2 concentrations, Fuel 88 (7) (2009) 1269–1274.

[7] S. Balusamy, A. Schmidt, S. Hochgreb, Flow field measurements of pulverized coal combustion using optical diagnostic techniques, Exp. Fluids 54 (2013) 1–14.

[8] S. Balusamy, S. Hochgreb, Flow field measurements of pulverized coal combustion in oxyfuel condition using laser diagnostic techniques, in: Proceedings of the European Combustion Meeting, 2013, pp. P5–15.

[9] K. Luo, H. Wang, J. Fan, F. Yi, Direct numerical simulation of pulverized coal combustion in a hot vitiated co-flow, Energy Fuels 26 (10) (2012) 6128–6136.

[10] T. Sayadi, S. Farazi, S. Kang, H. Pitsch, Transient multiple particle simulations of char particle combustion, Fuel 199 (2017) 289–298.

[11] T. Brosh, N. Chakraborty, Effects of equivalence ratio and turbulent velocity fluctuation on early stages of pulverized coal combustion following localized ignition: A direct numerical simulation analysis, Energy Fuels 28 (9) (2014) 6077–6088.

[12] T. Brosh, D. Patel, D. Wacks, N. Chakraborty, Numerical investigation of localised forced ignition of pulverised coal particle-laden mixtures: a direct numerical simulation (DNS) analysis, Fuel 145 (2015) 50–62.

[13] M. Muto, K. Yuasa, R. Kurose, Numerical simulation of ignition in pulverized coal combustion with detailed chemical reaction mechanism, Fuel 190 (2017) 136–144.

[14] G. Chen, H. Wang, K. Luo, J. Fan, A DNS study of pulverized coal combustion in a hot turbulent environment: Effects of particle size, mass loading and preferential concentration, Combust. Flame 254 (2023) 112839.

[15] K. Luo, C. Mao, J. Fan, Z. Zhuang, N.E.L. Haugen, Fully resolved simulations of single char particle combustion using a ghost-cell immersed boundary method, AIChE J. 64 (7) (2018) 2851–2863.

[16] H. Zhang, K. Luo, N.E.L. Haugen, C. Mao, J. Fan, Drag force for a burning particle, Combust. Flame 217 (2020) 188–199.

[17] S. Farazi, M. Sadr, S. Kang, M. Schiemann, N. Vorobiev, V. Scherer, H. Pitsch, Resolved simulations of single char particle combustion in a laminar flow field, Fuel 201 (2017) 15–28.

[18] T.R. Jayawickrama, N.E.L. Haugen, M.U. Babler, M.A. Chishty, K. Umeki, The effect of stefan flow on nusselt number and drag coefficient of spherical particles in non-isothermal gas flow, Int. J. Multiph. Flow 140 (2021) 103650.

[19] T.R. Jayawickrama, M.A. Chishty, N.E.L. Haugen, M.U. Babler, K. Umeki, The effects of stefan flow on the flow surrounding two closely spaced particles, Int. J. Multiph. Flow 166 (2023) 104499.

[20] G. Tufano, O. Stein, B. Wang, A. Kronenburg, M. Rieth, A. Kempf, Coal particle volatile combustion and flame interaction. Part I: Characterization of transient and group effects, Fuel 229 (2018) 262–269.

[21] F. Dierich, A. Richter, P. Nikrityuk, A fixed-grid model to track the interface and porosity of a chemically reacting moving char particle, Chem. Eng. Sci. 175 (2018) 296–305.

[22] J. Hees, D. Zabrodiec, A. Massmeyer, S. Pielsticker, B. Gövert, M. Habermehl, O. Hatzfeld, R. Kneer, Detailed analyzes of pulverized coal swirl flames in oxy-fuel atmospheres, Combust. Flame 172 (2016) 289–301.

[23] B. Franchetti, F.C. Marincola, S. Navarro-Martinez, A. Kempf, Large eddy simulation of a 100 kwth swirling oxy-coal furnace, Fuel 181 (2016) 491–502.

[24] T. Passot, A. Pouquet, Numerical simulation of compressible homogeneous flows in the turbulent regime, Journal of Fluid Mechanics 181 (1987) 441–466.

[25] L. Zhang, K. Liu, C. You, Fictitious domain method for fully resolved reacting gas–solid flow simulation, J. Comput. Phys. 299 (2015) 215–228.

[26] K. Luo, Z. Zhuang, J. Fan, N.E.L. Haugen, A ghost-cell immersed boundary method for simulations of heat transfer in compressible flows under different boundary conditions, Int. J. Heat Mass Transfer 92 (2016) 708–717.

[27] M. Uhlmann, An immersed boundary method with direct forcing for the simulation of particulate flows, J. Comput. Phys. 209 (2) (2005) 448–476.

[28] S. Tschisgale, T. Kempe, J. Fröhlich, A general implicit direct forcing immersed boundary method for rigid particles, Comput. & Fluids 170 (2018) 285–298.

[29] A. Brandenburg, A. Johansen, P.A. Bourdin, W. Dobler, W. Lyra, M. Rheinhardt, S. Bingert, N.E.L. Haugen, A. Mee, F. Gent, et al., The pencil code, a modular MPI code for partial differential equations and particles: multipurpose and multiuser-maintained, 2020, arXiv preprint arXiv:2009.08231.

[30] X.J. Liu, L. Li, Numerical studies on the combustion properties of char particle clusters, Int. J. Heat Mass Transfer 52 (21–22) (2009) 4785–4795.

[31] N.G. Deen, S.H. Kriebitzsch, M.A. van der Hoef, J. Kuipers, Direct numerical simulation of flow and heat transfer in dense fluid–particle systems, Chem. Eng. Sci. 81 (2012) 329–344.

[32] P. Bagchi, K. Kottam, Effect of freestream isotropic turbulence on heat transfer from a sphere, Phys. Fluids 20 (7) (2008).

[33] L. Botto, A. Prosperetti, A fully resolved numerical simulation of turbulent flow past one or several spherical particles, Phys. Fluids 24 (1) (2012).

[34] L. Schiller, A drag coefficient correlation, Zeit. Ver. Deutsch. Ing. 77 (1933) 318–320.